# *Radiative Enhancement of Plasmonic Nanopatch Antennas*

**Zilong Wu & Yuebing Zheng**

**Plasmonics**

ISSN 1557-1955

Plasmonics
DOI 10.1007/s11468-015-0043-y


Springer

Plasmonics
DOI 10.1007/s11468-015-0043-y

# Radiative Enhancement of Plasmonic Nanopatch Antennas

**Zilong Wu**[1] · **Yuebing Zheng**[1,2]

Received: 15 May 2015 / Accepted: 26 July 2015


**Abstract** Efficient light manipulation at subwavelength scale is of great interest for solar energy conversion, optical sensing, and nanophotonic devices. Recently, plasmonic nanopatch antennas (PNAs), which consist of plasmonic nanoparticles and metal films with thin layers of dielectric spacers sandwiched between them, have shown promise for directing and enhancing radiation from the dipole emitters at the PNAs. Herein, we apply finite-difference time-domain simulations to comparatively study the radiative enhancement of a series of PNAs consisting of Ag nanoparticles with different geometries, i.e., nanosquare, nanotriangle, nanorod, and nanodisk. We find that the shape of the Ag nanoparticles influences the resonant wavelength of the plasmonic waveguide modes in the spacers, the enhancement of localized electric field, and multiple aspects of the radiation, including spontaneous emission rate, quantum efficiency, and radiative enhancement factor. Nanodisk-based PNAs exhibit both high quantum efficiency (~0.74) and radiative enhancement factor (>20), while nanotriangle-based PNAs show remarkable spontaneous emission rate enhancement (>2500). Furthermore, we examine the effects of dipole emitter locations on the radiative properties. Our results pave the way towards the rational design of PNAs for the optimal plasmonic enhancement of light emission for targeted applications.

**Keywords** Plasmonic nanopatch antennas · Plasmonic waveguide modes · Purcell effects · Quantum efficiencies

## Introduction

Plasmonic nanostructures, which support the strong light-coupled coherent oscillations of free electrons (i.e., surface plasmon resonances), have attracted interests for manipulating light at the nanoscale [1–7]. With their capacity of enhancing the far-field light scattering and the near-field confinement of electromagnetic fields, plasmonic nanostructures have been used in a wide range of optoelectronic and photonic applications, such as plasmonic sensing [8–15], multi-photon lithography [16], single photon sources [17], plasmonic lenses [18–23], super absorbers [24–26], plasmonic lasers [27], solar energy conversion [28–33], and light-emitting diodes [34–36]. While many applications simply employ single plasmonic nanoparticles or ensembles of randomly distributed nanoparticles, recent years have witnessed ever-increasing research interests in the complex plasmonic nanostructures consisting of multiple properly coupled sub-units [37–41].

By introducing the plasmonic coupling effects in the complex nanostructures, one can enhance or even achieve new light-controlling capabilities. For example, nanoparticle dimers [42], in particular, bowtie nanostructures [43, 44], can achieve extremely high light concentration within the gaps between the nanoparticle pairs. The plasmon resonant wavelength can also be tuned by controlling the gap width [45]. Nanoparticle arrays that support collective plasmon modes have shown narrow bandwidth for plasmonic sensors of high figure-of-merit [46]. Recently, plasmonic nanopatch antennas

**Electronic supplementary material** The online version of this article (doi:10.1007/s11468-015-0043-y) contains supplementary material, which is available to authorized users.

✉ Yuebing Zheng
zheng@austin.utexas.edu

[1] Materials Science and Engineering Program, Texas Materials Institute, The University of Texas at Austin, Austin, TX 78712, USA

[2] Department of Mechanical Engineering, The University of Texas at Austin, Austin, TX 78712, USA

Published online: 07 August 2015

(PNAs), which consist of metal nanoparticles and metal films with thin layers of dielectric materials sandwiched between them (i.e., spacers), have attracted strong interests [47–49]. Unlike bowtie nanostructures that require sophisticated e-beam lithography or focused ion beam lithography to control the gaps and the plasmonic coupling, PNAs are compatible with the high-throughput thin film processing with the thickness of the spacers controllable down to the atomic layer [50].

The optical properties of PNAs are strongly correlated with the plasmonic waveguide modes (PWMs) in the metal-insulator-metal (MIM) structures [51–55]. The plasmon resonance peak wavelength associated with the PWMs can be tuned by controlling the thickness of the spacers, the lateral dimension of the metal nanoparticles, or the refractive index of spacer materials [56]. The PWMs also lead to the strong confinement of electromagnetic fields within the spacers with a large enhancement factor [57]. In addition, the PNAs have shown high radiation directionality [56]. Because many types of PNAs consisting of different nanoparticles exhibit variable properties, the rational design of the PNAs is highly desired in order to achieve the optimal performances for any targeted applications such as solar energy conversion, biomedical sensing, or nanophotonic light sources. Along this line, establishment of the structure-property relations for the PNAs consisting of different nanoparticles is required, which has not been available yet.

Herein, we perform numerical analysis for four types of PNAs consisting of commonly used Ag nanoparticles (i.e., nanosquare, nanotriangle, nanodisk, and nanorod) on Ag thin films with dielectric spacers of refractive index $n=1.4$. We comparatively analyze the effects of the nanoparticle geometry on the far- and near-field properties of PNAs and the radiative properties of dipole emitters at the PNAs. Based on our analysis, we suggest the preferred PNAs for different applications. Our study paves the way towards establishing the design rules for the PNAs for the optimal performance in the targeted applications.

## Methods

We perform numerical simulations using finite-different time-domain (FDTD) method. The commercially available software package (FDTD Solutions, Lumerical) is used. Figure 1 illustrates the schematics of the four types of PNAs used in our study. The nanoparticles in the PNAs include nanosquare, nanotriangle, nanodisk, and nanorod. Accordingly, we indicate these PNAs as square-, triangle-, disk-, and rod-PNAs, respectively. For each PNA, a dielectric spacer with a refractive index $n=1.4$ is sandwiched between the Ag nanoparticle and the Ag thin film. The PNA is supported by a glass substrate ($n=1.47$). The optical constant of Ag is obtained from reference [58]. The thickness of spacers and Ag films is set as 15 and 50 nm, respectively. For the scattering study, a normal ($\theta=0$ in Fig. 1) incident light is illuminated from the top of the PNAs and back-scattered light is collected with a two-dimensional (2D) frequency domain power detector at the top. For the radiative study, an electric dipole emitter is placed inside the spacer as illustrated in Fig. 1a. The light emitted by the dipole is collected using a small cube box consisting of six power detectors surrounding the dipole. The light radiated to the far field is measured in the same way using a large cube detector box surrounding the PNA. For all the simulations, the structures are modeled with a mesh size of 0.5 nm.

## Results and Discussion

### Plasmonic Waveguide Modes

Due to their critical role in the performance of PNAs, the PWMs of different types of PNAs are studied. For this purpose, a normal incident light is applied to excite the PWMs in the PNAs and the scattered light is analyzed. Figure 2 shows the simulated scattering spectra of the four types of PNAs. For the Ag nanoparticles in the PNAs, we set as 80 nm the lateral edge length of nanosquare, the equilateral edge of nanotriangle, the diameter of nanodisk, and the axial length of nanorod. All the nanoparticles have the same vertical thickness (along the $z$ direction) of 30 nm (see Fig. 1). The resonant wavelength of the PNAs is highly sensitive to the shape of the nanoparticles, ranging from 589 to 657 nm for our four cases. The inset of Fig. 2 shows a representative cross-sectional view of the electric field distribution for a square-PNA excited at the resonant peak wavelength. Due to the excitation of PWM, the incident optical power is strongly confined inside the spacer between the Ag nanoparticle and the Ag film, leading to two *hot spots* at the edges of the nanoparticle. The other three types of PNAs share the similar cross-sectional electric field distributions to the square-PNA (not shown here). The electric field distributions also reveal that the PWMs arise from the Fabry-Pérot resonances in the spacers [59]. The Fabry-Pérot resonances are responsible for the difference in the resonant wavelength of different PNAs due to the variation in the effective waveguide lengths.

To further investigate the effects of the PWMs on the near-field light confinement within the spacers of the PNAs, we analyze the lateral distributions of the electric field amplitude enhancement ($|E/E_0|$) at the central $x$-$y$ planes of the spacers as shown in Fig. 3. Hot spots with the highest enhancement appear beneath the corners or edges of the nanoparticles along the polarization direction of the incident light. These hot spots arise from the waveguide cavity modes, which are common for the MIM structures [59, 51, 52]. The excited PWMs and hot spots depend on the polarization direction of the incident light. The hot spots are located at two corners of the triangle-

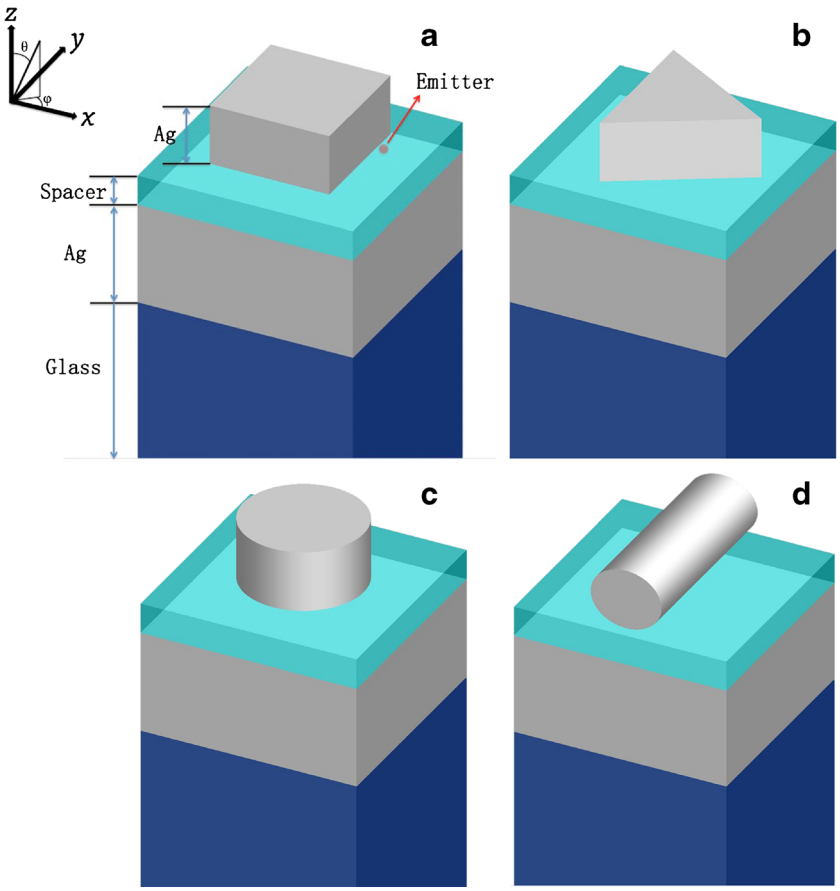


**Fig. 1** Schematics of four types of PNAs consisting of different Ag nanoparticles, i.e., **a** square-, **b** triangle-, **c** disk-, and **d** rod-PNAs

PNA when the polarization of incident light is aligned along one edge of the equilateral triangle. However, for the PWMs excited by dipole emitters incorporated within the spacer of a triangle-PNA, the hot spots appear at all of the three corners of the triangle. This unique property of triangle-PNAs will be further discussed in "Purcell Effect" section. The electric field enhancement is increased from the central *x*-*y* plane to the plane at the proximity of the nanoparticles (i.e., along the *z* direction), as shown in the inset of Fig. 2. Comparatively, triangle- and rod-PNAs support hot spots with the field enhancements (~80) higher than those of square- and disk-PNAs. The higher field enhancements in triangle- and rod-PNAs arise from their stronger light confinement as evidenced by the smaller areas of the hot spots.

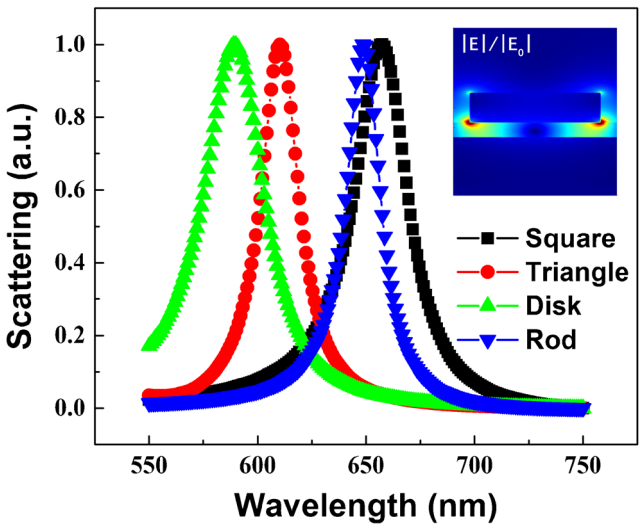


**Fig. 2** Simulated scattering spectra of four types of PNAs where the nanoparticles have the same lateral and vertical dimensions (i.e., 80 and 30 nm, respectively). The intensity of the spectra is normalized. *Inset* shows a representative cross-sectional view of the electric field amplitude distribution in the spacer of a PNA

## Purcell Effect

An optical emitter at the proximity of a plasmonic nanostructure exhibits an enhanced spontaneous emission rate due to the increased local density of states (LDOS) of the emitter's environment [60]. Such an increase of spontaneous emission rate is known as Purcell effect, underpinning many optical applications such as plasmon-enhanced light sources and bio-imaging [61]. PNAs have exhibited remarkable Purcell enhancement for emitters incorporated in the spacers due to the existence of the hot spots [57, 56]. Herein, we comparatively study the Purcell effect in the four types of PNAs.

For the study, we choose fluorophore, Cy5, and model it as an electric dipole emitter. To allow a direct comparison of

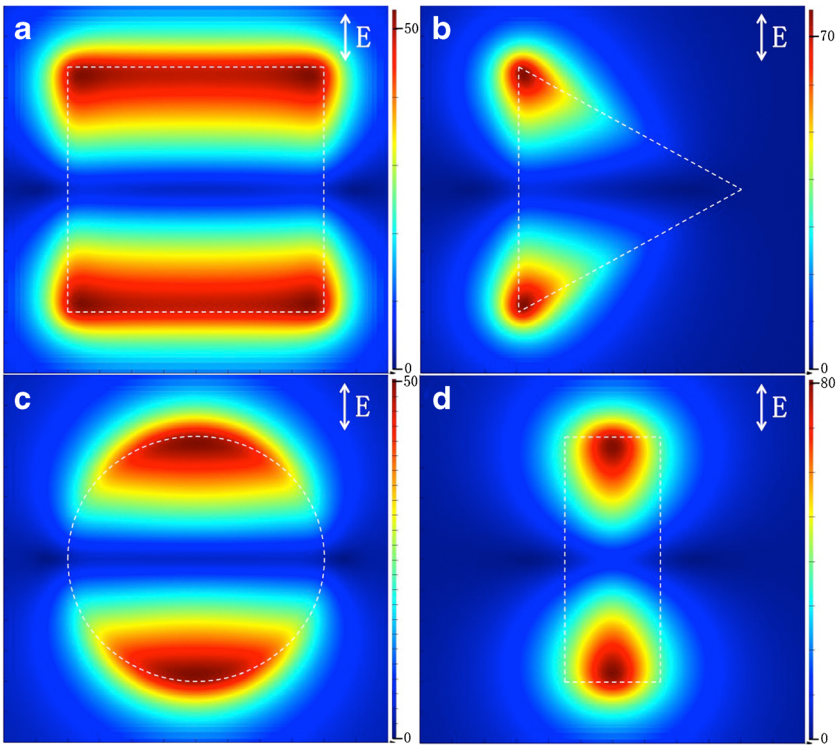


**Fig. 3** Lateral maps of electric field amplitude enhancement $|E/E_0|$ through the central *x-y* planes of spacers of the four types of PNAs. The projected profiles of the nanoparticles onto the *x-y* planes are indicated by *dash lines* (**a** square-, **b** triangle-, **c** disk-, and **d** rod-PNAs)

Purcell effects among the four types of PNAs, we tune the lateral dimensions of the nanoparticles to have the same resonant peak wavelength at 661 nm (Fig. S1), matching the emission peak wavelength of Cy5. The spontaneous emission rate enhancement, i.e., Purcell factor (PF), is calculated as $\gamma_{sp}/\gamma_{sp}^0 = P_{em}/P_{em}^0$ [62, 56], where $\gamma_{sp}$ and $\gamma_{sp}^0$ are the spontaneous emission rates of a dipole located within the spacer of a PNA and the bulky homogeneous dielectric environment, respectively. $P_{em}$ and $P_{em}^0$ are the optical powers emitted by the dipole located within the spacer of a PNA and the bulky homogeneous dielectric environment, respectively. In our FDTD simulations, we position single dipoles along the *x-y* plane that is 3 nm beneath the bottom edges of the nanoparticles to experience the highly enhanced electric field while avoiding the strong fluorescence quenching by the metal nanoparticles [56]. We set the orientation of the dipoles along the *z* direction because the *z* component of the electric field associated with the PWMs is much higher than the *x* and *y* components [56].

Figure 4 shows the PFs of the four types of PNAs as a function of the lateral position of the dipoles (i.e., along the *x-y* plane that is 3 nm beneath the bottom edges of the nanoparticles). For all the PNAs, the highest Purcell enhancements occur to the dipoles near the corners of the nanoparticles where the hot spots lead to the highest LDOS. For the dipoles at the center of the *x-y* plane, the PFs approach to 0 due to the extremely low electric field enhancement. The maximum PF for the four types of PNAs varies. The triangle-PNA has the maximum PF of ~12,000, which is highest among the PNAs, enabling the development of the high-frequency light sources. The difference in the maximum PF arises from the variation of maximum LDOS among the different PNAs. The lateral field distribution and maximum PF value (~4000) of square-PNA in Fig. 4a match well with those of the Ag cube-PNAs reported by Akselrod et al. [56]. According to our simulations in Fig. 4, the maximum Purcell enhancement of triangle-PNA is three times that of square-PNA. As a result, we expect that our proposed triangle-PNA can improve spontaneous emission rate more than the Ag cube-PNAs.

To further investigate the coupling between the emitters and the PWMs for the different types of PNAs, we map the electric field distributions along the *x-y* planes within the spacers upon the excitation of the emitters (Fig. 5). The dipole emitters with their orientation along the *z* direction are placed at the locations with the maximum PFs. Start apodization (with apodization center of 100 fs and apodization time width of 40 fs) is applied to filter away the strong and short-lived transient electric fields that occur when the dipole emitters are excited. Upon the optical excitation, the spontaneous emission of the dipoles couples to the PWMs of the PNAs, leading to two equally strong hot spots along the waveguide direction. The hot spots match those of the PWMs that are directly excited by normal incident light (Fig. 3). In addition, we find that the coupling of the emitted light to the PWMs is highly selective. For example, the emitted light by the dipole at one corner of the square-PNA selectively couples to the diagonally propagating PWMs (Fig. 5a). For the triangle-PNA, the spontaneous emission of the

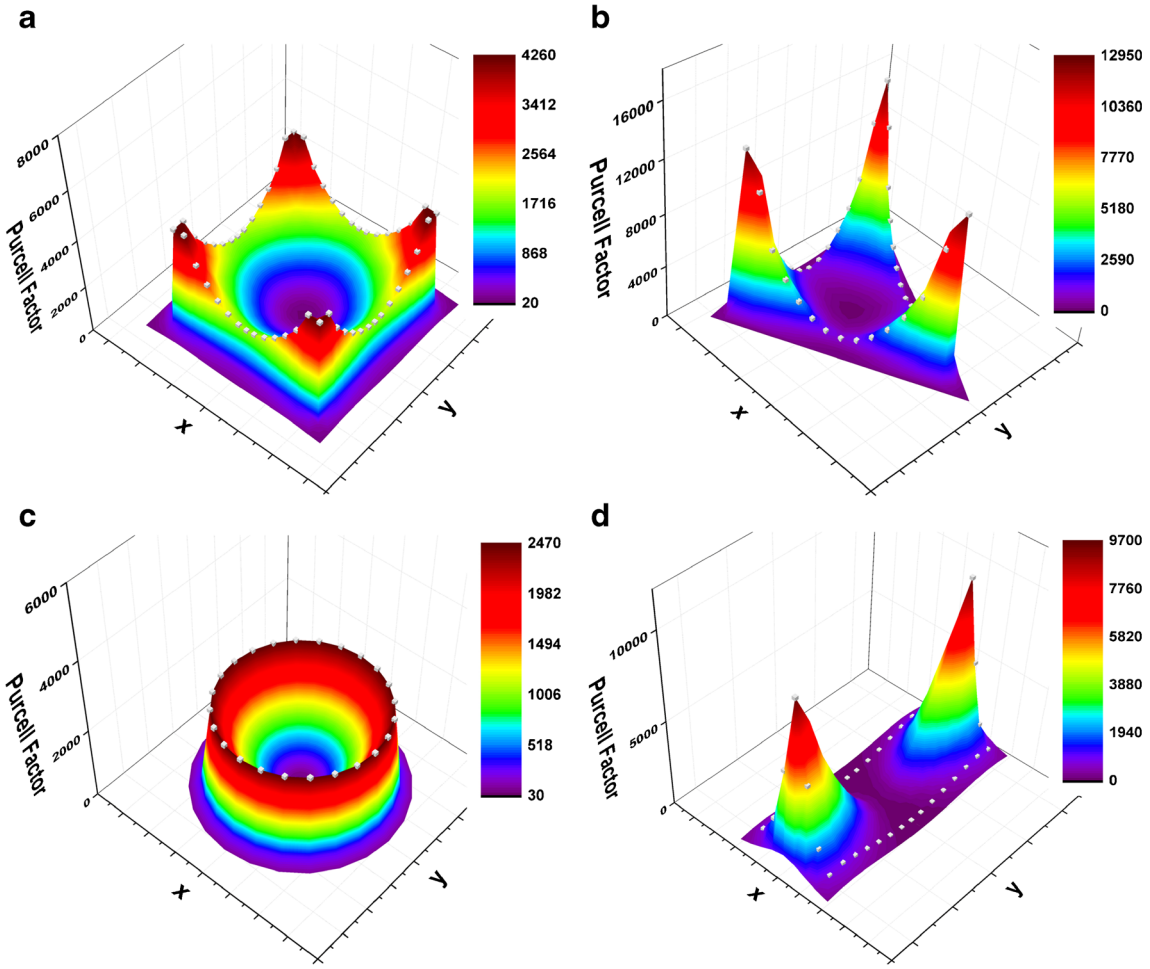


**Fig. 4** Purcell factors of the four types of PNAs as a function of dipole position. The profiles of the nanoparticles are indicated by *white dotted lines*, which are curved in the *z* direction (**a** square-, **b** triangle-, **c** disk-, and **d** rod-PNAs)

dipole is coupled to two PWMs along the two side edges due to the threefold symmetry of the triangle (Fig. 5b). Our simulations provide a new insight into how the light emitted by dipoles in spacers is concentrated and propagating within the waveguides of PNAs. We further reveal the dependence of dipole-PWM coupling on the shape of the nanoparticles in PNAs. Our findings can guide on the rational design of the location of emitters in the PNAs to achieve the strongest coupling between the emitted light and PWMs for improved photonics and optoelectronics.

To study the LDOS inside the spacers of the four types of PNAs shown in Fig. 5, we apply the normal incident light to directly excite the PWMs rather than using the dipole emitters. The polarizations of the incident light align with the directions of the PWMs that are excited by the dipole emitters in Fig. 5. The *z*-component amplitude of the electric fields in the spacers of the four types of PNAs is shown in Fig. S2. The match of variation within the hot spots between Fig. 4 and Fig. S2 confirms the correlations between the maximum LDOS and the maximum PFs.

## Radiative Quantum Efficiency

Radiative quantum efficiency (QE), which indicates the portion of emitted light propagating to the far field, is another important parameter for the applications of PNAs. Depending on the interactions between the emitters and the PNAs, the light emission can be either enhanced or quenched, leading to high or low QE, respectively. Herein, we systematically study the QE for the four types of PNAs.

In general, for an emitter at the proximity of a metal surface, radiative QE can be calculated as the following [62]:

$$\mathrm{QE} = \frac{\gamma_r \Big/ \gamma_r^0}{\gamma_r \Big/ \gamma_r^0 + \gamma_{abs} \Big/ \gamma_r^0 + (1-\eta^0) \Big/ \eta^0} \quad (1)$$

where $\gamma_r^0$ and $\eta^0$ are the intrinsic radiative decay rate and the intrinsic quantum yield of the emitter in homogeneous dielectric environment, respectively. $\gamma_r$ and $\gamma_{abs}$ are the radiative decay rate and the non-radiative decay rate (associated with the metal absorption) of the emitter near the metal surface, respectively. One defines $\gamma_r/\gamma_r^0 = P_r/P_r^0$ and $\gamma_{abs}/\gamma_r^0 = (P_{em} - P_r)/$

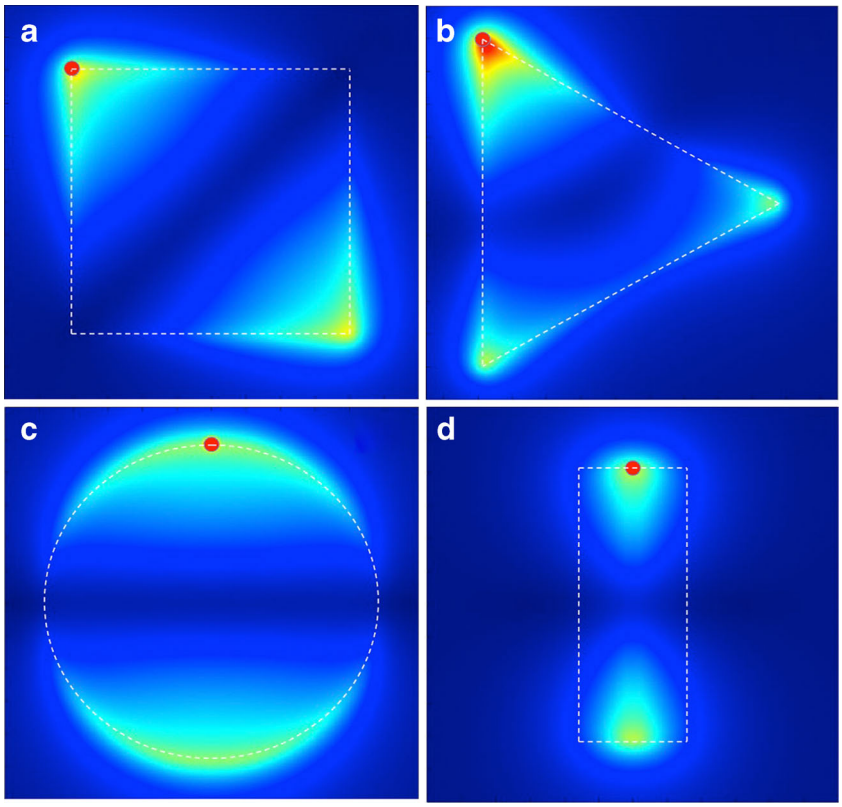


**Fig. 5** Lateral maps of electric field distribution in the spacers of four types of PNAs upon the excitation of the electric dipole emitters. The lateral positions of the emitters and the profiles of the nanoparticles in the PNAs are indicated by *small red circles* and *white dash lines*, respectively (**a** square-, **b** triangle-, **c** disk-, and **d** rod-PNAs)

$P_r^0$, where $P_r$ and $P_r^0$ are the powers radiated to the far field by a dipole emitter near a metal surface and in a homogeneous dielectric environment, respectively.

The intrinsic quantum yield of Cy5 molecules in homogeneous dielectric environment is 0.2 [57]. According to Eq. (1), we attain the lateral distributions of QE for the Cy5-based dipole emitters inside the spacers of the four types of PNAs as shown in Fig. 6. All the PNAs significantly enhance the QE with the highest enhancement at the edges of the nanoparticles where the strong interaction between the dipole emission and the PWMs occurs. The disk-PNA has the maximum QE that is 3.8 times the intrinsic quantum yield (0.2) of Cy5, indicating that about 76 % of the emitted photons from a dipole are radiated into the far field. The square-PNA exhibits the second highest maximum QE of 0.74. The triangle- and rod-PNAs have the lower maximum QEs of 0.62 and 0.52, respectively, which are still higher than the intrinsic ones.

For each type of PNA, the QE decreases from the edge to the center of the defined *x*-*y* plane beneath the nanoparticles as a result of both metal absorption and the coupling of dipole emission with PWMs. In general, when a dipole is moved from the edge to the center, the metal absorption increases and the enhancement of electric field amplitude decreases (Fig. 3). Near the edge of the nanoparticles, the electrical field enhancement dominates over the metal absorption, leading to a slight drop of QE. However, at the center, the localized electric field significantly decreases and the metal absorption dominates, causing a dramatic decrease of QE. As shown in Fig. 6d, the zigzag distribution of QE along the short axis through the middle of the length of the nanorod also arises from the competition between the electric field enhancement and the metal absorption.

## Radiative Enhancement Factor

Controlling the directionality of light emission from plasmonic nanostructures is important for their applications in single photon sources and molecular sensors [63]. PNAs exhibit the high directionality of light emission where the main slope of radiation from the dipoles inside the spacers is normal to the substrates (i.e., along the *z* direction in Fig. 1), and 84 % of the emitted light can be collected by an objective lens with a numerical aperture (NA) of 0.9 [57, 56]. Herein, we analyze the radiative enhancement factors (EFs) as collected by detectors with different NAs at the top surfaces of the four types of PNAs to gain insights into the light enhancement and the emission directionality.

The enhancement factor involving only the emission enhancement can be calculated as

$$\mathrm{EF} = \frac{\mathrm{QE} \times \mathrm{CE}}{\mathrm{QE}_0 \times \mathrm{CE}_0} \tag{2}$$

where CE is the collection efficiency (i.e., the fraction of photons collected by a detector over the total radiative light). The

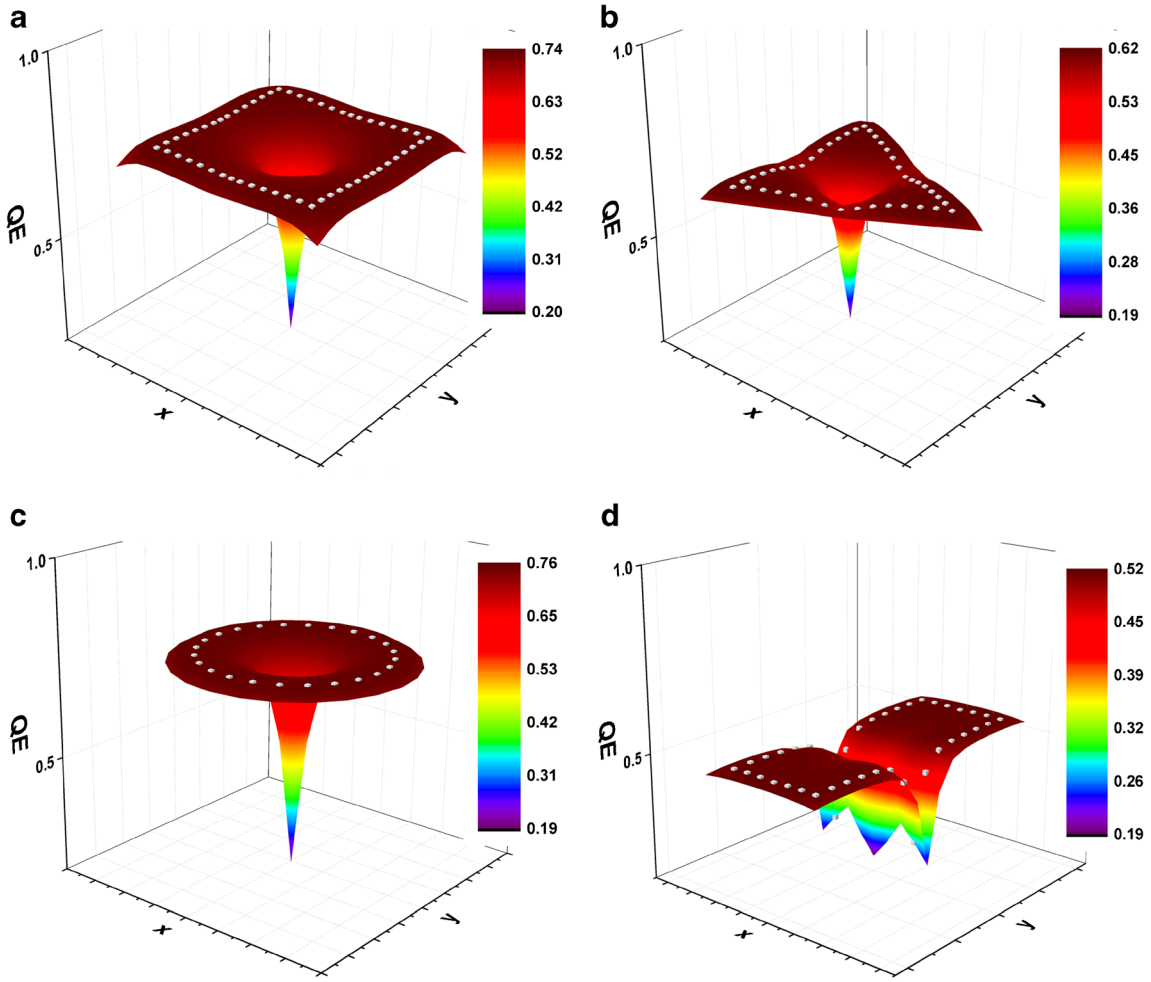


**Fig. 6** Radiative quantum efficiencies of four types of PNAs as a function of dipole emitter position. The profiles of the nanoparticles are illustrated by *white dotted lines*, which are curved in the *z* direction (**a** square-, **b** triangle-, **c** disk-, and **d** rod-PNAs)

subscript 0 in QE and CE represents the dipole in homogeneous dielectric environment. CE is obtained from FDTD simulations as

$$\mathrm{CE} = \int_0^{2\pi}\int_0^{\theta_{\max}} P_r(\theta,\varphi)\sin\theta d\varphi d\theta \Big/ \int_0^{2\pi}\int_0^{\pi/2} P_r(\theta,\varphi)\sin\theta d\varphi d\theta \tag{3}$$

where $\theta$ and $\varphi$ are angles as illustrated in Fig. 1, $P_r$ is the power radiated to the far field by a dipole emitter, and $\theta_{max} = \sin^{-1}(\mathrm{NA})$.

Figure 7 shows the calculated radiative EFs for the four types of PNAs as a function of the dipole emitter location when a lens of NA=0.1 is used to collect the emitted light from the top of the PNAs. The high EFs occur near the edges of the nanoparticles where the strong coupling between dipole emission and PWMs occurs. The disk-PNA has the maximum EF, and the dipoles near the edge of the nanodisk radiate into a solid angle of ~6° more than ~20 times the power of the dipoles in the homogeneous dielectric environment. The other three types of PNAs have the maximum EFs of over 14 when the dipoles are near the edges of the nanoparticles. The EFs for all the four types of PNAs decrease when the dipole emitter is moved from the edge to the center of the *x*-*y* plane beneath the nanoparticles, matching the spatial distributions of QEs. The good match between EFs and QEs confirms that the strong coupling between dipole emission and PWMs plays a dominant role in enhancing the light radiation into the far-field regions.

Besides the spatial distributions of the Purcell enhancement, QE, and EF, we further calculate the spatially averaged characteristics of these parameters for the four types of PNAs. The average characteristics are important for practical applications where emitters are often distributed broadly inside the spacers. In our calculations, the dipole emitters are uniformly distributed within the spacer areas that are equivalent to the lateral profiles of the nanoparticles. We still consider the dipoles that are oriented along the *z* direction due to the dominant *z*-component electric

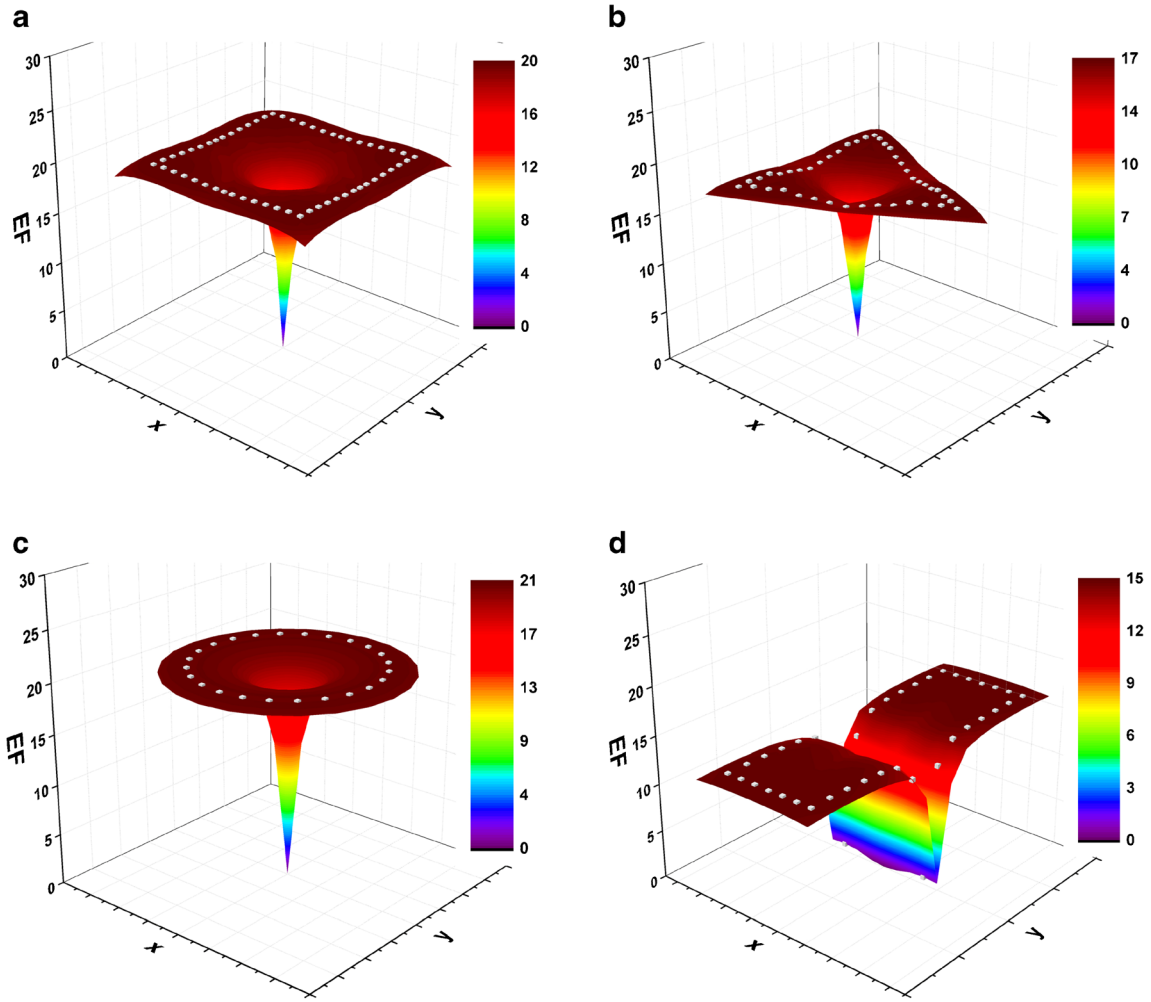


**Fig. 7** Radiative enhancement factors of the four types of PNAs as a function of dipole emitter position. The profiles of the nanoparticles are illustrated by *white dotted lines*, which are curved in the *z* direction (**a** square-, **b** triangle-, **c** disk-, and **d** rod-PNAs)

field in the PWMs. For our comparison, we also consider dipole emitters orientated along three orthogonal orientations (i.e., *x*, *y*, and *z* directions) in homogeneous dielectric environment. The overall enhancement factor ⟨EF⟩ is represented by $\langle QE \times CE / QE_0 \times CE_0 \rangle$.

Table 1 summarizes the spatially averaged characteristics for the four types of PNAs. The triangle-PNA has the highest spontaneous emission rate enhancement of over 2500 times that of the dipoles in homogeneous dielectric environment. With the high spontaneous emission rate enhancement and the quantum yield of ~0.6, the triangle-PNA is promising for applications in the high-frequency nanophotonic devices. The disk-PNA has a largest overall QE of 0.74, which is 3.7 times the intrinsic quantum yield of Cy5 molecules in homogenous dielectric environment. We calculate the overall EFs based on the collection lenses of different NAs (i.e., 0.1, 0.5, and 0.9). The disk-PNA has the highest overall EFs. The EFs increase when the NA is reduced, revealing the high emission directionality of all the PNAs.

**Table 1** A summary of spatially averaged characteristics of the four types of PNAs, including Purcell factor, quantum efficiency, and enhancement factors with different numerical apertures (NAs)

| | Purcell factor | Quantum efficiency | Enhancement factor (NA=0.1) | Enhancement factor (NA=0.5) | Enhancement factor (NA=0.9) |
|---|---|---|---|---|---|
| Triangle | 2596 | 0.59 | 16.3 | 15.2 | 12.9 |
| Square | 1592 | 0.71 | 19.8 | 18.3 | 15.6 |
| Rod | 1722 | 0.50 | 13.4 | 12.5 | 10.9 |
| Disk | 1489 | 0.74 | 20.5 | 18.9 | 16.2 |

## Conclusion

The geometry of the nanoparticles significantly impacts the scattering and emission properties of PNAs. By analyzing the PWMs, spontaneous emission rate enhancement, quantum efficiency, and radiative enhancement factor for the four types of PNAs with different nanoparticles (i.e., square-, triangle-, disk-, and rod-PNAs), we provide guidance on the choice of the optimal PNAs for some of the targeted applications. Disk-PNA is preferred for the applications that require high radiative quantum efficiency and radiative enhancement. Triangle-PNA enables high-frequency optical devices due to the remarkable spontaneous emission rate enhancement. With the extremely high spontaneous emission rate enhancement (>12, 000) near the corner of the nanotriangle, the triangle-PNA will enable the development of single-photon source operating at terahertz frequency. The further comparative study of the PNAs consisting of various nanoparticles and spacers will pave the way towards establishing the first set of design rules for the optimal implementation of these unique plasmonic nanostructures in a broad range of applications.

**Acknowledgments** The authors acknowledge the financial support of the Beckman Young Investigator Program and 3M Nontenured Faculty Award. We also acknowledge the Texas Advanced Computing Center (TACC) at The University of Texas at Austin for providing the HPC resources that have contributed to the research results reported within this paper. URL: http://www.tacc.utexas.edu.

## References

1. Liu Y, Zhang X (2011) Metamaterials: a new frontier of science and technology. Chem Soc Rev 40(5):2494–2507
2. Dragan AI, Bishop ES, Casas-Finet JR, Strouse RJ, McGivney J, Schenerman MA, Geddes CD (2012) Distance dependence of metal-enhanced fluorescence. Plasmonics 7(4):739–744
3. Mali B, Dragan AI, Karolin J, Geddes CD (2013) Photophysical characterization and α-type delayed luminescence of rapidly prepared Au clusters. J Phys Chem C 117(32):16650–16657
4. Lakowicz JR (2005) Radiative decay engineering 5: metal-enhanced fluorescence and plasmon emission. Anal Biochem 337(2):171–194
5. Zhang J, Matveeva E, Gryczynski I, Leonenko Z, Lakowicz JR (2005) Metal-enhanced fluoroimmunoassay on a silver film by vapor deposition. J Phys Chem B 109(16):7969–7975
6. Lin L, Zheng Y (2015) Multiple plasmonic-photonic couplings in the Au nanobeaker arrays: enhanced robustness and wavelength tunability. Opt Lett 40(9):2060–2063
7. Wang M, Zhao C, Miao X, Zhao Y, Rufo J, Liu YJ, Huang TJ, Zheng Y (2015) Plasmofluidics: Merging Light and Fluids at the Micro-/Nanoscale. Small.
8. Morton SM, Jensen L (2011) A discrete interaction model/quantum mechanical method to describe the interaction of metal nanoparticles and molecular absorption. J Chem Phys 135(13):134103
9. Payton JL, Morton SM, Moore JE, Jensen L (2012) A discrete interaction model/quantum mechanical method for simulating surface-enhanced raman spectroscopy. J Chem Phys 136(21): 214103
10. Moore JE, Morton SM, Jensen L (2012) Importance of correctly describing charge-transfer excitations for understanding the chemical effect in SERS. J Phys Chem Lett 3(17):2470–2475
11. Zhao C, Liu Y, Yang J, Zhang J (2014) Single-molecule detection and radiation control in solutions at high concentrations via a heterogeneous optical slot antenna. Nanoscale 6(15):9103–9109
12. Shao L, Ruan Q, Jiang R, Wang J (2014) Macroscale colloidal noble metal nanocrystal arrays and their refractive index-based sensing characteristics. Small 10(4):802–811
13. Aslan K, Geddes CD (2009) Wavelength-ratiometric plasmon light scattering-based immunoassays. Plasmonics 4(4):267–272
14. Zheng YB, Kiraly B, Weiss PS, Huang TJ (2012) Molecular plasmonics for biology and nanomedicine. Nanomedicine (London) 7(5):751–770
15. Li H, Chen DX, Sun YL, Zheng YB, Tan LL, Weiss PS, Yang YW (2013) Viologen-mediated assembly of and sensing with carboxylatopillar[5]arene-modified gold nanoparticles. J Am Chem Soc 135(4):1570–1576
16. Ueno K, Juodkazis S, Shibuya T, Yokota Y, Mizeikis V, Sasaki K, Misawa H (2008) Nanoparticle plasmon-assisted two-photon polymerization induced by incoherent excitation source. J Am Chem Soc 130(22):6928–6929
17. Filter R, Slowik K, Straubel J, Lederer F, Rockstuhl C (2014) Nanoantennas for ultrabright single photon sources. Opt Lett 39(5):1246–1249
18. Zhao C, Zhang J, Liu Y (2014) Light manipulation with encoded plasmonic nanostructures. EPJ Appl Metamaterials 1:6
19. Ma C, Liu Z (2011) Designing super-resolution metalenses by the combination of metamaterials and nanoscale plasmonic waveguide couplers. J Nanophotonics 5(1):051604
20. Zhao C, Liu Y, Zhao Y, Fang N, Huang TJ (2013) A reconfigurable plasmofluidic lens. Nat Commun 4.
21. Wan W, Ma C, Liu Z (2013) Control the dispersive properties of compound plasmonic lenses. Opt Commun 291:390–394
22. Ma C, Liu Z (2012) Breaking the imaging symmetry in negative refraction lenses. Opt Express 20(3):2581–2586
23. Liu Y, Zentgraf T, Bartal G, Zhang X (2010) Transformational plasmon optics. Nano Lett 10(6):1991–1997
24. Cui Y, Xu J, Hung Fung K, Jin Y, Kumar A, He S, Fang NX (2011) A thin film broadband absorber based on multi-sized nanoantennas. Appl Phys Lett 99(25):253101
25. Cui Y, Fung KH, Xu J, Ma H, Jin Y, He S, Fang NX (2012) Ultrabroadband light absorption by a sawtooth anisotropic metamaterial slab. Nano Lett 12(3):1443–1447
26. Cui Y, Fung KH, Xu J, He S, Fang NX (2012) Multiband plasmonic absorber based on transverse phase resonances. Opt Express 20(16):17552–17559
27. Ma RM, Ota S, Li Y, Yang S, Zhang X (2014) Explosives detection in a lasing plasmon nanocavity. Nat Nanotechnol 9(8):600–604
28. Beliatis MJ, Henley SJ, Han S, Gandhi K, Adikaari AA, Stratakis E, Kymakis E, Silva SR (2013) Organic solar cells with plasmonic layers formed by laser nanofabrication. Phys Chem Chem Phys 15(21):8237–8244
29. Catchpole K, Polman A (2008) Plasmonic solar cells. Opt Express 16(26):21793–21800
30. Atwater HA, Polman A (2010) Plasmonics for improved photovoltaic devices. Nat Mater 9(3):205–213
31. Fang C, Jia H, Chang S, Ruan Q, Wang P, Chen T, Wang J (2014) (Gold core)/(titania shell) nanostructures for plasmon-enhanced photon harvesting and generation of reactive oxygen species. Energy Environ Sci 7(10):3431–3438
32. Hu Z, Yu JC, Ming T, Wang J (2015) A wide-spectrum-responsive $TiO_2$ photoanode for photoelectrochemical cells. Appl Catal B Environ 168–169:483–489
33. Sun C, Su J, Wang X (2015) A design of thin film silicon solar cells based on silver nanoparticle arrays. Plasmonics 10(3):633–641

34. Schietinger S, Barth M, Aichele T, Benson O (2009) Plasmon-enhanced single photon emission from a nanoassembled metal–diamond hybrid structure at room temperature. Nano Lett 9(4):1694–1698
35. Geddes C, Lakowicz J (2002) Editorial: metal-enhanced fluorescence. J Fluoresc 12(2):121–129
36. Gryczynski I, Malicka J, Jiang W, Fischer H, Chan WC, Gryczynski Z, Grudzinski W, Lakowicz JR (2005) Surface-plasmon-coupled emission of quantum dots. J Phys Chem B 109(3):1088–1093
37. Passarelli N, Pérez LA, Coronado EA (2014) Plasmonic interactions: from molecular plasmonics and fano resonances to ferroplasmons. ACS Nano 8(10):9723–9728
38. Suh JY, Kim CH, Zhou W, Huntington MD, Co DT, Wasielewski MR, Odom TW (2012) Plasmonic bowtie nanolaser arrays. Nano Lett 12(11):5769–5774
39. Meinzer N, Barnes WL, Hooper IR (2014) Plasmonic meta-atoms and metasurfaces. Nat Photonics 8(12):889–898
40. Klinkla R, Pinsook U, Boonchui S (2015) Role of symmetry in coupled localized surface plasmon resonance of a nanosphere pair. Plasmonics 10(3):643–653
41. Lin L, Zheng Y (2015) Engineering of parallel plasmonic-photonic interactions for on-chip refractive index sensors. Nanoscale
42. Perez-Gonzalez O, Zabala N, Aizpurua J (2014) Optical properties and sensing in plexcitonic nanocavities: from simple molecular linkers to molecular aggregate layers. Nanotechnology 25(3): 035201
43. Schuck PJ, Fromm DP, Sundaramurthy A, Kino GS, Moerner WE (2005) Improving the mismatch between light and nanoscale objects with gold bowtie nanoantennas. Phys Rev Lett 94(1):017402
44. Calderón J, Álvarez J, Martinez-Pastor J, Hill D (2015) Polarimetric plasmonic sensing with bowtie nanoantenna arrays. Plasmonics 10(3):703–711
45. Hatab NA, Hsueh C-H, Gaddis AL, Retterer ST, Li J-H, Eres G, Zhang Z, Gu B (2010) Free-standing optical gold bowtie nanoantenna with variable gap size for enhanced raman spectroscopy. Nano Lett 10(12):4952–4955
46. Vecchi G, Giannini V, Gómez Rivas J (2009) Shaping the fluorescent emission by lattice resonances in plasmonic crystals of nanoantennas. Phys Rev Lett 102(14):146807
47. Sorger VJ, Pholchai N, Cubukcu E, Oulton RF, Kolchin P, Borschel C, Gnauck M, Ronning C, Zhang X (2011) Strongly enhanced molecular fluorescence inside a nanoscale waveguide gap. Nano Lett 11(11):4907–4911
48. Esteban R, Teperik TV, Greffet JJ (2010) Optical patch antennas for single photon emission using surface plasmon resonances. Phys Rev Lett 104(2):026802
49. Belacel C, Habert B, Bigourdan F, Marquier F, Hugonin JP, de Vasconcellos SM, Lafosse X, Coolen L, Schwob C, Javaux C, Dubertret B, Greffet JJ, Senellart P, Maitre A (2013) Controlling spontaneous emission with plasmonic optical patch antennas. Nano Lett 13(4):1516–1521
50. Atay T, Song J-H, Nurmikko AV (2004) Strongly interacting plasmon nanoparticle pairs: from dipole–dipole interaction to conductively coupled regime. Nano Lett 4(9):1627–1631
51. Gordon R (2006) Light in a subwavelength slit in a metal: propagation and reflection. Phys Rev B 73(15):153405
52. Dionne JA, Sweatlock LA, Atwater HA, Polman A (2006) Plasmon slot waveguides: towards chip-scale propagation with subwavelength-scale localization. Phys Rev B 73(3):035407
53. Dionne JA, Lezec HJ, Atwater HA (2006) Highly confined photon transport in subwavelength metallic slot waveguides. Nano Lett 6(9):1928–1932
54. Alaee R, Menzel C, Huebner U, Pshenay-Severin E, Bin Hasan S, Pertsch T, Rockstuhl C, Lederer F (2013) Deep-subwavelength plasmonic nanoresonators exploiting extreme coupling. Nano Lett 13(8):3482–3486
55. Frederiksen M, Bochenkov VE, Ogaki R, Sutherland DS (2013) Onset of bonding plasmon hybridization preceded by gap modes in dielectric splitting of metal disks. Nano Lett 13(12):6033–6039
56. Akselrod GM, Argyropoulos C, Hoang TB, Ciracì C, Fang C, Huang J, Smith DR, Mikkelsen MH (2014) Probing the mechanisms of large Purcell enhancement in plasmonic nanoantennas. Nat Photonics 8:835–840
57. Rose A, Hoang TB, McGuire F, Mock JJ, Ciraci C, Smith DR, Mikkelsen MH (2014) Control of radiative processes using tunable plasmonic nanopatch antennas. Nano Lett 14(8):4797–4802
58. Johnson PB, Christy R-W (1972) Optical constants of the noble metals. Phys Rev B 6(12):4370
59. Chandran A, Barnard ES, White JS, Brongersma ML (2012) Metal-dielectric-metal surface plasmon-polariton resonators. Phys Rev B 85(8):085416
60. Anger P, Bharadwaj P, Novotny L (2006) Enhancement and quenching of single-molecule fluorescence. Phys Rev Lett 96(11): 113002
61. Purcell EM (1946) Spontaneous emission probabilities at radio frequencies. Phys Rev 69:681
62. Bauch M, Dostalek J (2013) Collective localized surface plasmons for high performance fluorescence biosensing. Opt Express 21(17): 20470–20483
63. Kosako T, Kadoya Y, Hofmann HF (2010) Directional control of light by a nano-optical Yagi-Uda antenna. Nat Photonics 4(5):312–315